



HAL
open science

One-dimensional capillary jumps

Médéric Argentina, Alexandre Cohen, Yann Bouret, Nathalie Fraysse,
Christophe Raufaste

► **To cite this version:**

Médéric Argentina, Alexandre Cohen, Yann Bouret, Nathalie Fraysse, Christophe Raufaste. One-dimensional capillary jumps. *Journal of Fluid Mechanics*, 2015, 765, pp.1 - 16. 10.1017/jfm.2014.717 . hal-01111202

HAL Id: hal-01111202

<https://hal.science/hal-01111202>

Submitted on 29 Jan 2015

HAL is a multi-disciplinary open access archive for the deposit and dissemination of scientific research documents, whether they are published or not. The documents may come from teaching and research institutions in France or abroad, or from public or private research centers.

L'archive ouverte pluridisciplinaire **HAL**, est destinée au dépôt et à la diffusion de documents scientifiques de niveau recherche, publiés ou non, émanant des établissements d'enseignement et de recherche français ou étrangers, des laboratoires publics ou privés.

One dimensional capillary jumps

Médéric Argentina^{1,3} †, A. Cohen², Y. Bouret², N. Fraysse² and C. Raufaste²

¹Université Nice Sophia Antipolis, CNRS, INLN UMR 7335, 06560 Valbonne, France

²Université Nice Sophia Antipolis, CNRS, LPMC UMR 7336, 06100 Nice, France

³Institut Universitaire de France, 75005 Paris, France

(Received ?; revised ?; accepted ?. - To be entered by editorial office)

In flows where the ratio inertia to gravity varies strongly, large variations in the fluid thickness appear and hydraulic jumps arise, as depicted by Rayleigh. We report a new family of hydraulic jumps, where the capillary effects dominate the gravitational acceleration. The Bond number -which measures the importance of gravitational body forces to surface tension- must be small in order to observe such objects using capillarity as a driving force. For water, the typical length should be smaller than 3 mm. Nevertheless, for such small scales, solid boundaries induce viscous stresses which dominate inertia, and capillary jump shall not be described by the inertial shock wave theory that one would deduce from Bélanger or Rayleigh for hydraulic jumps. In order to get rid of viscous shears, we consider Plateau borders, which are the microchannels defined by the merging of three films inside liquid foams, and we show that capillary jumps propagate along these deformable conduits. We derive a simple model which predicts the velocity, the geometry and the shape of such fronts. A strong analogy with the Rayleigh's description is pointed out. In addition, we carried out experiments on a single Plateau border generated with soap films to observe and characterize these capillary jumps. Our theoretical predictions agree remarkably well with the experimental measurements.

Key words: Authors should not enter keywords on the manuscript, as these must be chosen by the author during the online submission process and will then be added during the typesetting process (see <http://journals.cambridge.org/data/relatedlink/jfm-keywords.pdf> for the full list)

1. Introduction

Hydraulic jumps are waves which connect sections of strongly varying flows. They were observed by famous authors, including Leonardo da Vinci, Savart (1833), Bidone (1819), Bélanger (1841) and Rayleigh (1914). The last two ones introduced the well known conservation laws at the jump for mass and momentum, Rayleigh being able to derive these from a continuous description of the thickness profile. At the position of the jump, the flow speed, v , decreases drastically from supersonic to subsonic with respect to the local surface wave speed. In a thin layer of height h , the speed of gravity waves is given by \sqrt{gh} , where g is the acceleration due to gravity. The corresponding dimensionless number is the Froude number, $Fr = v/\sqrt{gh}$, where the velocity v is defined with respect to the reference frame where the hydraulic jump is standing. The flow upstream of the jump, being more rapid than the surface waves, is referred to as supercritical with $Fr > 1$, while

† Email address for correspondence: mederic.argentina@unice.fr

the flow downstream of the jump is referred to as subcritical with $Fr < 1$. This allows the vision of the hydraulic jump as a shock-wave, in analogy with compressible gas flows (Lighthill (1978)), and in which a hypothetical transition would be localized at a place where $Fr = 1$. The Mach cone, which is a characteristic of supercritical flows, has been observed in radial hydraulic jumps by Jannes *et al.* (2011), who suggested a possible transition governed by $Fr = 1$ at the jump position. In rivers, hydraulic jumps, whose position is almost stationary, appear because of variations of the river bed (Chow (1959), Simpson (1997)). The tidal bores, which are wavefronts associated to a tide propagating in opposite direction to the river current can also be interpreted as moving hydraulic jumps (Chanson (2011)). These natural objects, which share the same characteristic high Reynolds number, Re , do exhibit turbulent flows that provide strong variations of the surface profile.

In order to probe moderately high Reynolds number flows, hydraulic jumps might be created by impacting a jet on a solid surface, as in the commonly operation of opening the tap of a kitchen sink. The obtained hydraulic jump takes a circular form whose radius depends on the viscosity (Watson (1964), Craik *et al.* (1981), Bohr *et al.* (1993)), and is not directly given by the $Fr = 1$ criterion (applied to a hypothetical inertial flow that in fact never holds). At the centimeter scale and in this geometry, the formation mechanism appears to be a coupling between the boundary layer emerging from the solid substrate and the free surface (Watson (1964), Bowles & Smith (1992), Higuera (1994)). Craik *et al.* (1981) partially observed the existence of a reverse flow which takes the form of a toroidal vortex and acts like a springboard for the incoming fluid. This separation of the boundary layer might be explained by the existence of an adverse pressure gradient, as proposed Tani (1949) and Kurihara (1946). Theoretical approaches (Watson (1964), Bohr *et al.* (1997), Rojas *et al.* (2010)) and numerical techniques (Yokoi & Xiao (2002), Passandideh-Fard *et al.* (2011)) have also evidenced this peculiar flow. Various scaling laws predict a viscosity dependence for the radius position (Watson (1964), Bohr *et al.* (1997), Bush & Aristoff (2003), Rojas *et al.* (2013), Duchesne *et al.* (2014)). In addition, experimental measurements of Duchesne *et al.* (2014) show the occurrence at the exit of circular hydraulic jumps of a locked value of the Froude number, whose value is independent of the flow rate imposed by the jet. One dimensional hydraulic jumps, which have been addressed by Bonn *et al.* (2008), are slightly different, since the upstream fluid thickness increases almost linearly in space. The hydraulic jumps created by the impact jet present the advantage of being almost laminar, but the formation mechanism appears to be also deeply linked to viscous effects.

We describe here a new kind of hydraulic jumps, where the driving force has a capillary origin, gravitational effects can be omitted, and viscosity does not play a fundamental role in the formation mechanism. In a thin layer of thickness l , the characteristic surface wave velocity behaves as $\sqrt{\frac{\gamma}{\rho l}}$, where ρ is the density of the fluid and γ its surface tension. In such a case, the Froude number introduced in the Rayleigh theory is replaced by the Weber number $We = \frac{\rho v^2 l}{\gamma}$. Consequently, there exists a critical Weber number We_c under which surface waves cannot travel faster than the fluid flow. A capillary driven hydraulic jump is expected in flows for which $We - We_c$ changes its sign. This scenario should be potentially observed in thin films falling down an inclined plane, as depicted by Kapitza (1948), in which capillary effects might dominate gravity. Nevertheless, the small length scale also introduces notable viscous shear, which affects the shock-wave criterion.

In this article, we present capillary hydraulic jumps, analogous to hydraulic jumps, formed in a Plateau border (PB). The Plateau's laws describe the geometric properties of interacting soap films. At equilibrium, they always meet in threes, creating a mi-

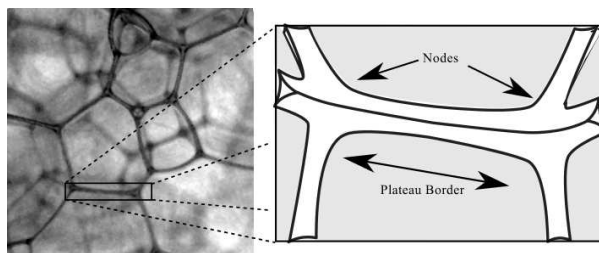


FIGURE 1. Optical photograph of a liquid foam. The close up shows a Plateau border. The gray areas represent the liquid films shared by two adjacent bubbles.

crochannel, called Plateau Border (See Fig. 1). PBs merge into nodes and the PBs-nodes network creates a porous medium which mediates the liquid flows. Usually, the drainage in the gravitational field can be described using low Reynolds flows in a Darcy like approach (Weaire *et al.* (1993), Koehler *et al.* (1999)). In capillary suction experiments, the flow is triggered by capillary effects due to PB thickness inhomogeneities. In that case, the Ohnesorge number $Oh = \frac{\sqrt{We}}{Re}$ discriminates different regimes for the fluid flow (Cohen *et al.* (2014)). We have used here $Re = \rho vl/\eta$, where the fluid viscosity is η . For $Oh > 0.05$, PB perturbations disappear through viscous damping, whereas for $Oh < 0.05$, inertia dominates the flow and a wave, similar to a hydraulic jump, propagates along the PB with an almost constant velocity. This is the regime we address in this study.

This article is organized as follows. Section 2 describes a simple model for capillary jumps in PBs. The comparison between our theoretical predictions and our experimental measurements are presented in section 3. In section 4, we propose an energetic argument providing a selection mechanism of the capillary jumps.

2. Model

The model aims at computing the shape and velocity of the capillary jump. We consider the Plateau border depicted in Fig. 2.a: the three holding films are attached to a triangular prism frame. The liquid flows along the z axis. R_{ext} defines the radius of the circumcircle of the equilateral triangles defining the holding frame (see Fig. 2.b).

The interior region delimited by the arcs \widehat{AB} , \widehat{BC} and \widehat{CA} defines the PB channel. We assume a constant pressure P_{ext} in the surrounding air. Laplace's law predicts the radius of curvature of the arcs as $R = \gamma/(P_{ext} - P)$, such that the cross section of the PB is symmetric since all the surfaces of the channel share the same curvature. γ is the surface tension and P the pressure inside the fluid. The channel thickness $e = \frac{\sqrt{3}}{2}R$ is defined as the height of the equilateral triangle ABC . The segments AA' , BB' and CC' represent the three films composed of two interfaces separating the fluid from the air.

We note $\mathcal{P} = \pi R$ the PB perimeter and $\mathcal{A} = \alpha R^2$ its cross section area, with $\alpha = \sqrt{3} - \frac{\pi}{2}$. The length \mathcal{L} of the interfaces on the cross section is the sum of the perimeter \mathcal{P} and six times the distance AA' (the factor two arises because each film is composed of two liquid-air interfaces):

$$\mathcal{L} = -2\alpha R + 6R_{ext}. \quad (2.1)$$

As consequence, the area of the liquid-air interfaces of the system decreases as R increases, as pointed out by G eminard *et al.* (2004). The PB capillary energy, proportional to \mathcal{L} ,

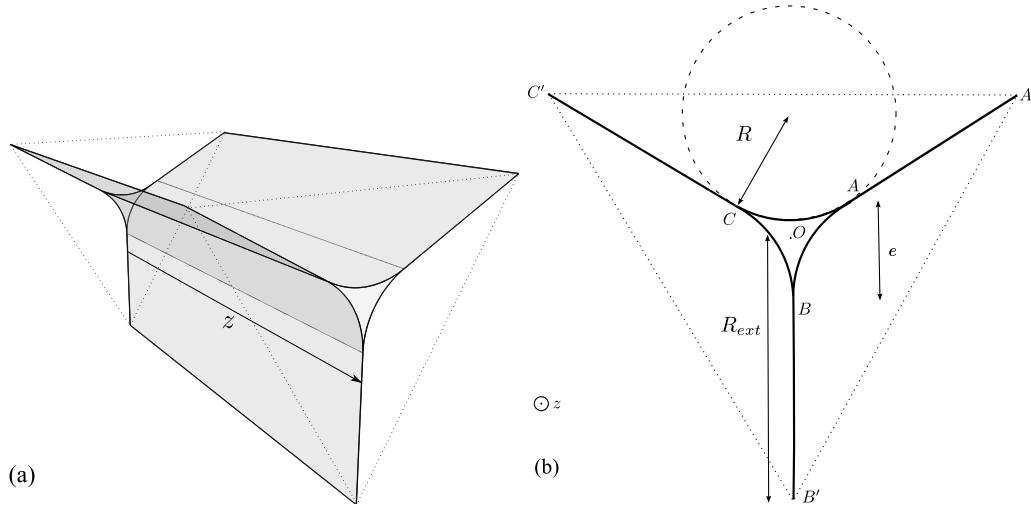


FIGURE 2. (a) Three-dimensional representation of the system. The gray surfaces represent the liquid-air interfaces. The dashed lines represent equilateral triangles with a circumcircle of radius R_{ext} (b) Arbitrary cross section of the system showing the Plateau border with its three holding films. The thick curves represent liquid-air interfaces. The thickness, e , of the PB is proportional to its radius of curvature, R .

decreases as the PB thickness e increases. From an energetic point of view, the PB tends to increase its size e , which is a necessary condition for the capillary jump existence.

The model derivation is based on the following assumptions:

- The flow is laminar and characterized by a high Reynolds number.
- The pressure P and the longitudinal velocity u inside the channel only depend on z .
- The variations of all the physical variables are small in the z direction.

The jump propagates with a constant velocity of amplitude c towards a region where the fluid velocity is zero and $R = R_i$. Experimentally, the injection of fluid inside the PB, initially at rest with $R = R_i$, might create the jump as the fluid excess propagates (see the section 3).

The system is described in the reference frame of the capillary jump, where the flow is steady, as shown in Fig. 3. With the variable Z attached to the reference frame of the front ($Z = z - ct$, with z the variable in the laboratory frame), the mass conservation writes

$$\partial_Z (uA) = 0, \quad (2.2)$$

where we have neglected the mass flow inside the films since their area in the cross section is negligible compared to A . We write the longitudinal momentum conservation in a slice of fluid between Z and $Z + dZ$:

$$\partial_Z [\mathcal{A}(\rho u^2 + P - P_{ext} - \sigma_{zz}) - \gamma \mathcal{L}] = 0. \quad (2.3)$$

The first term in the momentum flux arises from the flow inside the channel. Surface tension exerts a longitudinal force proportional to \mathcal{L} pointing outward the infinitesimal cylinder. Longitudinal flows inside the films have been neglected with respect to those inside the channel. $\sigma_{zz} = 2\eta\partial_Z u$ is the viscous shear stress applied to the cross section oriented in the Z direction. The fluid pressure P , evaluated at the fluid surface, obeys

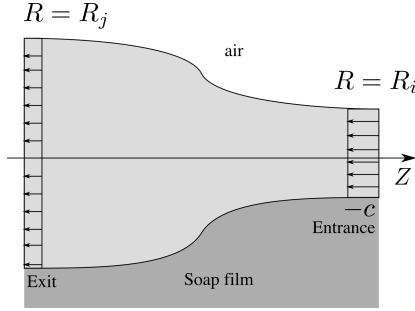


FIGURE 3. Longitudinal section of the capillarity jump, in its reference frame. The jump moves to the right with a velocity c in the laboratory frame.

the dynamic boundary condition:

$$P + \gamma\kappa = P_{ext} + \sigma_{rr}, \quad \text{on } \widehat{AB}, \widehat{BC}, \widehat{CA}, \quad (2.4)$$

valid in the limit of small longitudinal deformations of the interfaces. σ_{rr} is the normal fluid shear stress applied to the surface of the PB. The mean curvature κ writes :

$$\kappa = \frac{1}{R(Z)} + \beta_1 R''(Z) + \beta_2 \frac{R'(Z)^2}{R(Z)}, \quad (2.5)$$

obtained in the small slope limit (see the appendix A). $\beta_{1,2}$ are geometrical coefficients. To close the model, we compute an approximation of the viscous stress $\sigma_{rr} = 2\eta\partial_r u_r$, with u_r defined as the radial velocity. The fluid is incompressible, and we relate the radial velocity with the longitudinal velocity using the divergence-free flow relation following an idea developed by Bogoy (1979):

$$\frac{1}{r}\partial_r(ru_r) + \partial_Z u = 0, \quad (2.6)$$

where the angular dependence has been disregarded. Integrating this relation gives $u_r = -\frac{r}{2}\partial_Z u$. Consequently, the radial viscous stress approximates to:

$$\sigma_{rr} = -\eta\partial_Z u. \quad (2.7)$$

This rough approximation gives σ_{rr} which is similar to the radial shear stress in cylindrical jets. Inserting (2.1,2.4,2.5,2.7) into (2.3) yields:

$$\partial_Z \left[\mathcal{A} \left(\rho u^2 + \gamma \left(\frac{1}{R} - \beta_1 \partial_{ZZ} R - \beta_2 \frac{(\partial_Z R)^2}{R} \right) - 3\eta \partial_Z u \right) \right] = 0. \quad (2.8)$$

Note that the sign of the $1/R$ coefficient has changed with respect to the mean curvature expression (2.5), due to the tension induced by the holding films. These latter generate a homogeneous pressure as it is the case for cylindrical jets. The Eq. 2.8 is integrated into

$$\rho u^2 + \gamma \left(\frac{1}{R} - \beta_1 \partial_{ZZ} R - \beta_2 \frac{(\partial_Z R)^2}{R} \right) - 3\eta \partial_Z u = \frac{d}{R^2}, \quad (2.9)$$

where the integration constant d is determined by the boundary conditions.

Because of the Galilean invariance, we assume that, in the laboratory frame, the capillary jump propagates with a velocity c towards $z \rightarrow +\infty$, at which $R = R_i$, as shown in

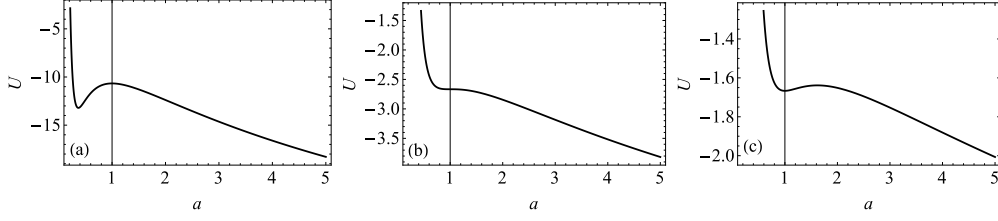


FIGURE 4. Dependence of the potential energy \mathcal{U} on We . (a) $We = 0.1$. (b) $We = 1/2$. (c) $We = 1$.

Fig. 3. The value of R at $z \rightarrow -\infty$ is named R_j . We summarize the boundary conditions:

$$u(\infty) = -c \quad (2.10)$$

$$R(-\infty) = R_j \quad (2.11)$$

$$R(\infty) = R_i. \quad (2.12)$$

Using R_i and c as the characteristic length and velocity of the system, we rescale the physical quantities $u = cv$, $R = R_i a$ and $Z = R_i s$. The set of equations (2.2,2.9) becomes

$$v = -\frac{1}{a^2} \quad (2.13)$$

$$\frac{1}{a^4} - \frac{d_2}{a^2} + \frac{1}{We} \left(\frac{1}{a} - \beta_1 \partial_{ss} a - \beta_2 \frac{(\partial_s a)^2}{a} \right) - \frac{1}{Re} \frac{6}{a^3} \partial_s a = 0, \quad (2.14)$$

where d_2 is the dimensionless integration constant arising from d . We have introduced the Reynolds number, Re and the Weber number We :

$$We = \frac{\rho c^2 R_i}{\gamma}, \quad Re = \frac{\rho c R_i}{\eta}. \quad (2.15)$$

The capillary jump velocity c is still an unknown. Two boundary conditions fix d_2 and We . Imposing (2.12) on Eq. (2.14) settles $d_2 = 1 + \frac{1}{We}$. The boundary condition (2.11) gives the following relation:

$$We = \tilde{r}^2 \frac{1}{1 + \tilde{r}}, \quad (2.16)$$

where we have introduced the ratio $\tilde{r} = \frac{R_j}{R_i}$. The capillary jump velocity is deduced from (2.15,2.16):

$$c = \sqrt{\frac{\gamma}{\rho R_i} \tilde{r} \frac{1}{\sqrt{1 + \tilde{r}}}}, \quad (2.17)$$

such that the propagation velocity is proportional to the capillary wave velocity $c_0 = \sqrt{\frac{\gamma}{\rho R_i}}$, and a geometrical factor which only depends on the ratio \tilde{r} . The Reynolds number defined in (2.15) becomes

$$Re = \frac{1}{Oh} \frac{\tilde{r}}{\sqrt{1 + \tilde{r}}}, \quad (2.18)$$

where $Oh = \frac{\eta}{\sqrt{\rho \gamma R_i}}$ is the Ohnesorge number, which is the ratio of viscous stresses induced by capillary waves, to inertia.

The Eq. (2.14) presents a nice analogy with the differential equations of mechanical nonlinear oscillators, since it may be written in the following form:

$$\frac{\beta_1}{We} \partial_{ss} a + f(a, Re, We) \partial_s a + \partial_a \mathcal{U} = 0. \quad (2.19)$$

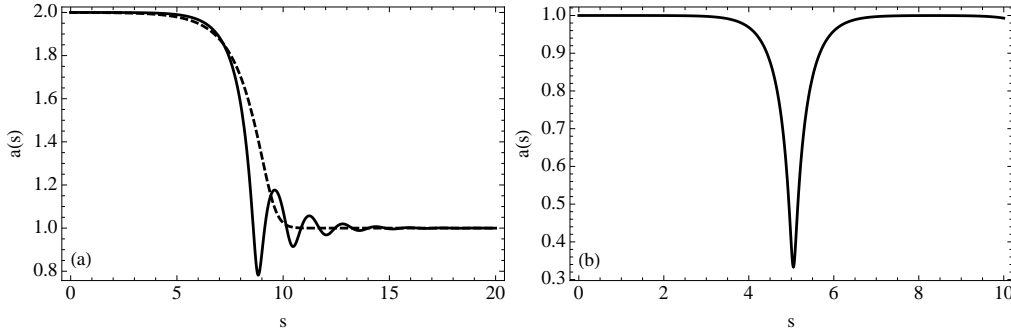


FIGURE 5. Plateau border profiles. (a) Capillary jumps numerically computed for $We = 4/3$ (equivalent to $\tilde{r} = 2$). Solid and dashed curves have been obtained for $Re = 60$ and $Re = 10$, respectively. (b) Solitary wave profile, for very low viscosities, obtained numerically from Eq. (2.24) with $We = 1/6$.

The dimensionless space variable s is analogous to the temporal variable t of oscillators. As usual, the first term represents the acceleration. A dissipation function appears in factor of $\partial_s a$: $f(a, Re, We) = \frac{6}{a^3 Re} + \beta_2 \frac{\partial_s a}{a We}$. This analogy suggests that $\mathcal{U} = \frac{1}{3a^3} - \frac{1+1/We}{a} - \ln(a)/We$ stands for an effective potential energy which is plotted in Fig. 4. The function \mathcal{U} has one maximum and one minimum, given the physical constraint $a > 0$.

2.1. Capillary jump

The capillary jump is the heteroclinic trajectory which connects two extrema of \mathcal{U} , namely for $a(-\infty) = R_j/R_i$ and $a(\infty) = 1$. As consequence, $a = R_j/R_i$ must be the position of the maximum of \mathcal{U} , whereas $a = 1$ must be the position of the finite minimum of \mathcal{U} . This last condition, $\partial_{aa}U|_{a=1} > 0$, turns into:

$$We > \frac{1}{2}. \quad (2.20)$$

The analogy with Rayleigh theory for hydraulic jumps becomes straightforward. A capillary jump with $R_j > R_i$ exists only if $We > 1/2$, which is equivalent to the supercritical criterion $Fr > 1$ for hydraulic jumps. Due to the oscillating nature of Eq. (2.19), undulations are expected during the relaxation of a to 1. Two numerical profiles are shown in Fig. 5.a. For low values of the Reynolds number, the viscous forces dominate the inertia, and a becomes monotonic. The oscillation wavelength is assessed from a linear analysis of Eq. (2.19) around $a = 1$ by studying the dynamics of a perturbation $b = a - 1$:

$$\frac{\beta_1}{We} \partial_{ss} b + \frac{6}{Re} \partial_s b + \left(2 - \frac{1}{We}\right) b = 0. \quad (2.21)$$

Since this equation is linear, imposing $b \sim e^{qs}$ yields:

$$q = -3 \frac{We}{\beta_1 Re} \pm i \frac{1}{\sqrt{\beta_1}} \sqrt{2We - 1} + o\left(\frac{1}{Re}\right)^2. \quad (2.22)$$

For small Reynolds number, viscosity damps oscillations as the real part of q becomes very high. The dimensional wavelength $\lambda = 2\pi/R_i \text{Im}(q)$ is:

$$\lambda = R_i \frac{2\pi\sqrt{\beta_1}}{\sqrt{2We - 1}} \quad (2.23)$$

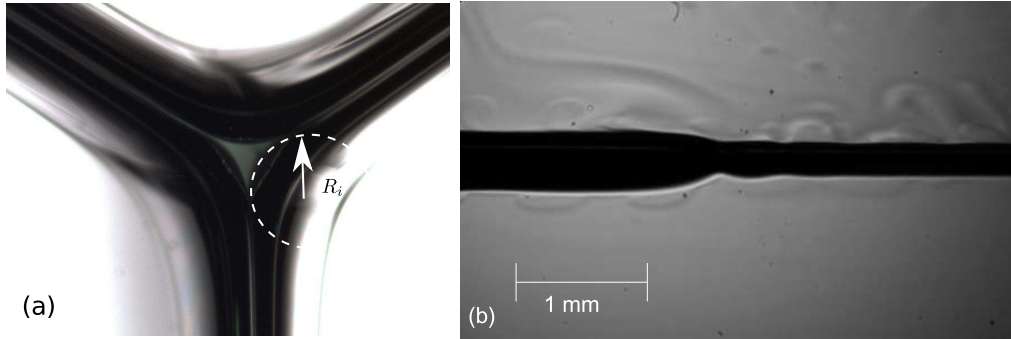


FIGURE 6. (a) Cross section of the unperturbed Plateau border. Here $R_i = 0.261\text{mm}$. (b) Longitudinal view of a propagating capillary jump on the Plateau border (solution (I)).

2.2. Solitary wave

In the case where viscous shear can be neglected, i.e. $Re \gg 1$, our model predicts the existence of solitary waves, which are homoclinic orbits connected to $a = 1$. In this parameter regime, the Eq. (2.14) multiplied by $a^2 \partial_s a$ and integrated with respect to the variable s , reduces to

$$\frac{a(s)^2 (1 - \beta a'(s)^2)}{2We} - \frac{(We + 1)a(s)}{We} - \frac{1}{a(s)} = E. \quad (2.24)$$

To derive the previous relation, we have assumed $\beta_1 = \beta_2 = \beta$, since β_1 and β_2 have almost the same numerical value (see Appendix A). The boundary conditions $a(\infty) = 1$ and $a'(\infty) = 0$ fix the value $E = -\frac{1+4We}{2We}$. Finally, the profile minimum $a_m = 2We$ is obtained by solving Eq. (2.24) with $a'(s) = 0$. A typical spatial profile of the solitary wave is shown in Fig. 5.b; its velocity is deduced from Eq. (2.16):

$$c = c_0 \sqrt{\frac{a_m}{2}}. \quad (2.25)$$

Physically, these waves take the form of a localized constriction of the Plateau border, traveling with a constant speed. A localized perturbation yielding a localized contraction might generate two of these solitary waves travelling in opposite directions. These structures are not connected to an external reservoir, like the previously described capillary jumps.

3. Experimental study

3.1. Materials and methods

In order to create the Plateau Border, we constructed a 15 mm long triangular-prism frame. After dipping it into a soapy solution, the PB appears in the longitudinal direction. The frame is positioned to settle the PB horizontally, and rotated around its longitudinal axis such that the channel profile adopts the Y shape shown in Figs. 2 and 6.a. We can vary the radius of curvature of the PB, R_i (see Fig. 6.a), by injecting liquid at one upper-corner of the frame. In this study, we have used two liquid solutions leading to tangential-stress free interfaces (Raufaste *et al.* (2009), Pitois *et al.* (2005)):

- Solution (I) was obtained by adding 5% of a commercial dishwashing liquid (Dreft, Procter & Gamble) to de-ionized water. The physical properties of solution (I) are $\rho = 980 \text{ kg.m}^{-3}$, $\gamma = 26 \text{ mN/m}$ and $\eta = 1.08 \text{ mPa.s}$.

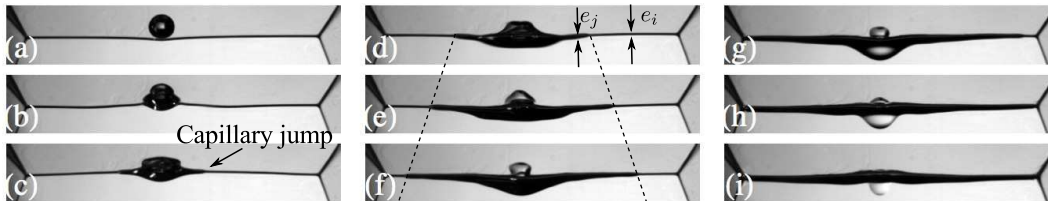


FIGURE 7. Snapshots of a Plateau border with two propagating capillary jumps. The pictures are recorded every 2.5 ms. (a) A droplet is released from above. (b) It coalesces with the PB. (c) Two capillary jumps are formed, one on each side of the droplet. (d-g) They propagate along the PB. (h) They reach the nodes. The two dashed lines are for guidance only, to show that a steady regime is reached.

- Solution (II) was obtained by dissolving TTAB (Tetradecyl trimethyl ammonium bromide) into de-ionized water.

The physical properties of solution (II) are $\rho = 1030 \text{ kg}\cdot\text{m}^{-3}$, $\gamma = 36 \text{ mN/m}$ and $\eta = 1.04 \text{ mPa}\cdot\text{s}$.

For both solutions, the density ρ was measured by weighing a known volume of solution (error of $\pm 50 \text{ kg/m}^3$), the dynamic viscosity η was determined using a Ubbelohde viscometer (error of $\pm 2\%$) and the surface tension γ was measured using the pendant drop method (error of $\pm 1 \text{ mN/m}$), as described in Hansen & Rødsrud (1991).

Experiments are backlit and recorded from the side by means of a high-speed camera (1000 - 2000 fps), in order to follow the temporal evolution of the Plateau border (Fig. 7). A calibration step is performed before each set of experiments, which consists in coupling cross section and longitudinal views, in order to deduce the radius of curvature R of the Plateau border from its apparent thickness, e ; This calibration gives $R_i = (1.08 \pm 0.02)e_i$.

3.2. Experimental results and comparison with the model

To create a capillary jump, we perturb the Plateau border by releasing a small droplet of the same surfactant solution from above, as seen in Fig. 7.a. After a transient time, a permanent regime installs and two propagative capillary jumps are created on both sides of the droplet, as pictured in Fig. 7. The droplet radius, which varies in our experiments from 0.2 to 1.8 mm, does not play a significant role in the characteristics of the capillary jumps (see Cohen *et al.* (2014)). As an example, we show in movie m1 a jump formation following the drop coalescence at one of the edge of the PB. After a short transient regime, observed on a length scale given approximately by the perturbation size, these structures propagate steadily with a constant velocity, c and exhibit small spatial oscillations near the jumps as shown in Fig. 6.b. This is illustrated by the movie m2 of the supplementary materials. A space-time diagram of the apparent PB thickness (Fig. 8.a) demonstrates that c remains constant during the propagation. This diagram was constructed as follows. The set of pictures (one example of picture is shown in Fig. 6b) extracted from a movie was binarized to discriminate the PB from the air. For each binarized picture, the liquid thickness profile is computed (one example is shown in Fig. 8b) and is associated to a grey scale. This settles the horizontal line for this given time in the space-time diagram.

3.2.1. Capillary jump profile

The PB profile exhibits damped spatial undulations upstream (see Fig. 6.b). These wavy deformations are stationary in the reference frame of the capillary jump, as shown in the space-time diagram of the PB thickness in Fig. 8a. To compare the experimental profile to our model, we use a Runge-Kutta method, precise at fourth order, as numerical

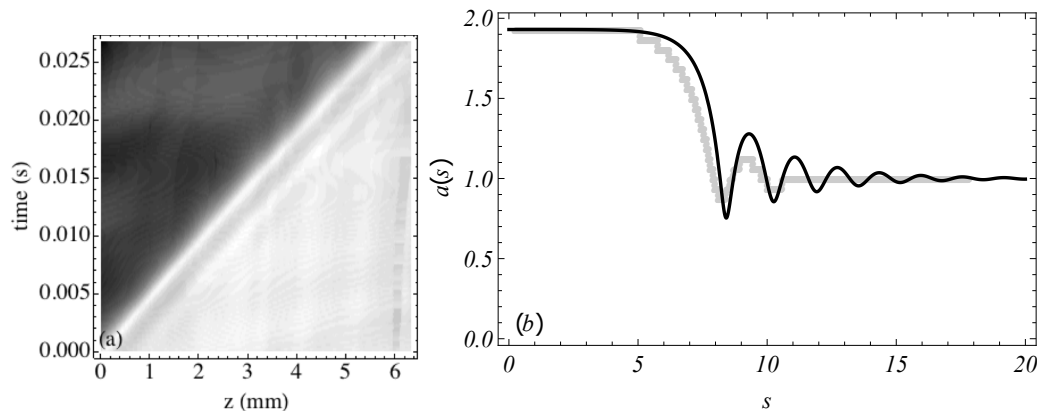


FIGURE 8. (a) Space-time diagram of the thickness of the capillary jump for solution (I). The darkest (lightest) color represents 0.582 mm (0.216 mm) for the thickness of the PB, respectively. (b) Comparison with the model of the capillary jump profile observed for the solution (I). Gray disks represent the experimental thickness of the PB measured optically and renormalized by the thickness e_i of the PB at the entrance. The experimental radii of curvature of the PB upstream and downstream of the jump are $R_i = 0.30$ mm, $R_j = 0.57$ mm, respectively; Eq. (2.16) gives $We = 1.35$; $Re = 95$, when computed with a velocity $c = 0.28$ m/s deduced from Eq. (2.17) and the physical values of solution (I). This sets the profile $a(s)$ (black curve) predicted by Eq. (2.14).

scheme (Press *et al.* (2007)). In order to compute the spatial evolution of $a(s)$, we first use the experimental values of R_i and R_j to obtain We through Eq. (2.16). The capillary-jump velocity c is computed from Eq. (2.17), and used to evaluate Re . The numerical profile is then computed via a shooting method with the initial boundary conditions $a(0) = R_j/R_i$ and $a'(0) = -\epsilon$. The small parameter ϵ controls the position of the capillary jump, but does not affect the shape of $a(s)$ since Eq. (2.14) is invariant under space translation. We choose ϵ in order to superimpose the profile onto the experimental one, as can be seen in Fig. 8b. The numerical integration of Eq. (2.14) matches very well with the experimental observation, although the model has been derived within a slender slope approximation. The model nicely captures the undulations together with the typical size of the jump. The dissipation model does not accurately predict the maxima of the oscillations: a much more precise description of the shear stresses including the angular dependence has to be developed. Nevertheless, our present model already captures the fundamental physics of the capillary jump.

3.2.2. Capillary jump aspect ratio

In Fig. 9a, we show the measured radius R_j of curvature of the PB downstream of the jump: for the two solutions (I) and (II). R_j is plotted as a function of the measured initial radius of curvature of the PB, R_i . For each liquid solution, the data-points coalesce onto a line. A linear regression gives $R_j = (1.93 \pm 0.03)R_i$ for solution (I) and $R_j = (1.54 \pm 0.03)R_i$ for solution (II). For each solution, the ratio R_j to R_i appears to be constant within a good accuracy. This aspect ratio is the input parameter of our model and sets the geometrical factor of Eq. (2.17) to 1.13 and 0.96, and the Weber number of Eq. (2.16) to 1.27 and 0.92 for solutions (I) and (II), respectively.

3.2.3. Capillary jump velocity

We measured the velocity of the jumps for solutions (I) and (II). Fig. 9b shows the dependence of the jump velocity on R_i . For both solutions, a linear regression of the ex-

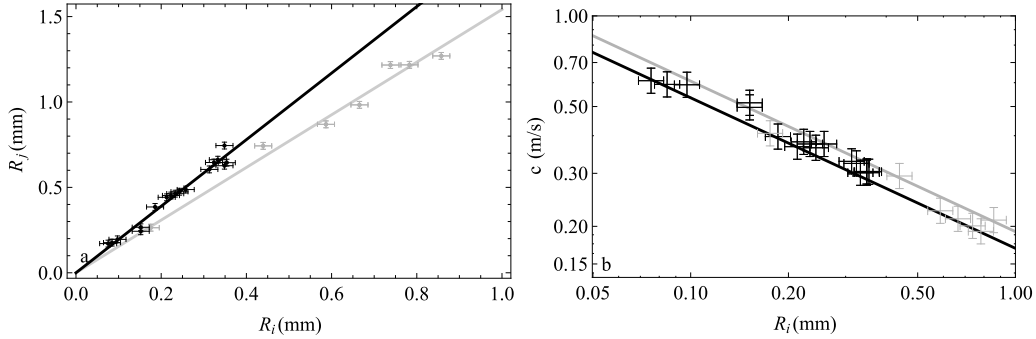


FIGURE 9. (a) R_j vs R_i , measured for solution (I) (black markers) and solution (II) (gray markers). The black and gray curves respectively represent $R_j/R_i = 1.93$ and $R_j/R_i = 1.54$. (b) Velocity of the capillary jump as function of R_i (logarithmic scales), measured on solution (I) (black markers) and solution (II) (gray markers). The black and gray solid lines are the velocity predictions using Eq.(2.17) for each data set.

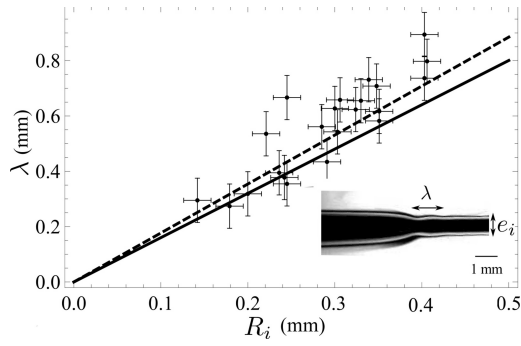


FIGURE 10. Wavelength λ vs R_i , measured on capillary jumps observed for solution (I). The dashed line represents the best linear fit $\lambda = (1.78 \pm 0.1) R_i$. The continuous line $\lambda = 1.6 R_i$ stands for the model prediction of Eq. (2.23).

perimental points yields a scaling with a power law -0.50 for the jump velocity. The Fig. 9b, shows the remarkable agreement between our model prediction and the experimental measurements.

3.2.4. Upstream undulations

As observed by Craik *et al.* (1981) in radial hydraulic jumps, capillary waves might decorate the jump rim, in the supercritical regime. The capillary jump shares this property. These steady undulations travel with the structure. We have measured the wavelength, λ , in experiments with liquid solution (I) and are reported in Fig. 10. The best linear fit gives $\lambda = (1.8 \pm 0.02) R_i$ whereas our model predicts $\lambda = 1.6 R_i$, and slightly underestimates the experimental wavelengths.

4. Selection mechanism of the capillary jump

In all that precedes, the capillary jump aspect ratio R_j/R_i was required as an input parameter for the model to retrieve the experimental observations : jump profile, front velocity, undulations wavelengths. Experimentally, this aspect ratio is found to be independent on the size of the released droplet (data not shown), and thus constant for a given liquid solution. In what follows, we assume that the jump is self-adapting in shape

independently of the perturbation that created it and we show that a simple energetic argument predicts the value R_j/R_i chosen by the system. The excess of energy injected at $\pm\infty$ is viscously dissipated within the whole channel. Following Landau & Lifshitz (1987), the energy balance is written

$$\left[\mathcal{A}u \left(\frac{\rho u^2}{2} + (P - P_{ext}) \right) + \gamma \mathcal{L}u \right]_{-\infty}^{\infty} = - \int_{-\infty}^{\infty} \int_{\mathcal{A}} \Phi d\mathcal{A}dz, \quad (4.1)$$

where Φ is the viscous dissipation per unit volume. For a Newtonian fluid, this term writes in cylindrical coordinates: $\Phi = \eta[2(\partial_z u)^2 + 2\left(\frac{u_r}{r}\right)^2 + 2(\partial_r u_r)^2 + (\partial_r u + \partial_z u_r)^2]$, which becomes $\Phi = \eta[3(\partial_z u)^2 + \frac{1}{4}R^2(\partial_{zz}u)^2]$ within the approximation $r \simeq R$. In dimensionless variables, Eq. (4.1) is written:

$$\left[\frac{1}{2a^4} + \frac{1}{We} \frac{1}{a} \right]_{-\infty}^{\infty} = \frac{12}{Re} I(Oh, \tilde{r}) \quad (4.2)$$

$$I(Oh, \tilde{r}) = \int_{-\infty}^{\infty} \left(\frac{1}{a^2} \partial_s a \right)^2 + \frac{1}{48} \left(a^2 \partial_{ss} \frac{1}{a^2} \right)^2 ds, \quad (4.3)$$

For a given ratio R_j/R_i , the Weber number can be computed by use of Eq. (2.16), while c is predicted through Eq.(2.17).

The differential equation (2.14) is then controlled through the ratio $\tilde{r} = R_j/R_i$ and Oh . The same holds for the profile of the capillary jump and its associated integral (4.3). We reduce the Eq. (4.2) to an equation for the unknown \tilde{r} :

$$\frac{(1 + \tilde{r})^{\frac{5}{2}}(\tilde{r} - 1)}{2\tilde{r}^3} = 12OhI(Oh, \tilde{r}). \quad (4.4)$$

Solving the previous equation gives the curvature radius ratio R_j/R_i selected by the droplet-mediated jump creation. The integral (4.3) can be evaluated numerically using a simple trapezoidal integration of the profile computed with Eq. (2.14). In Fig. 11.a, we plot the l.h.s and the r.h.s of Eq. (4.4).

In Fig. 11.b, we show the dependence of the numerically computed ratio \tilde{r} with respect to Oh . R_j/R_i tends to 1.934 for small Oh values. For the liquid solutions (I) and (II), we experimentally visited the range $0.01 < Oh < 0.02$ and $0.005 < Oh < 0.008$ respectively, and the values of R_j/R_i were measured to be 1.93 and 1.54 respectively. The small discrepancy can be explained by additional dissipative sources. In our model, the surface shear has been disregarded and this assumption might not be valid for all classes of surfactant, as described by Buzza *et al.* (1995). Given that the predicted value is obtained by integrating over the whole PB profile, with no free parameter, the agreement is very satisfactory.

For the highest values of Oh , the selected R_j/R_i value tends to be very high. Unfortunately this regime cannot be tested experimentally since no capillary jumps were observed for $Oh \geq 0.05$ (Cohen *et al.* (2014)). From that value of Oh , the capillary jump geometry is broken and the comparison with the model is no longer possible. We add that our model can not predict this transition since the geometry is prescribed to the one of a capillary jump.

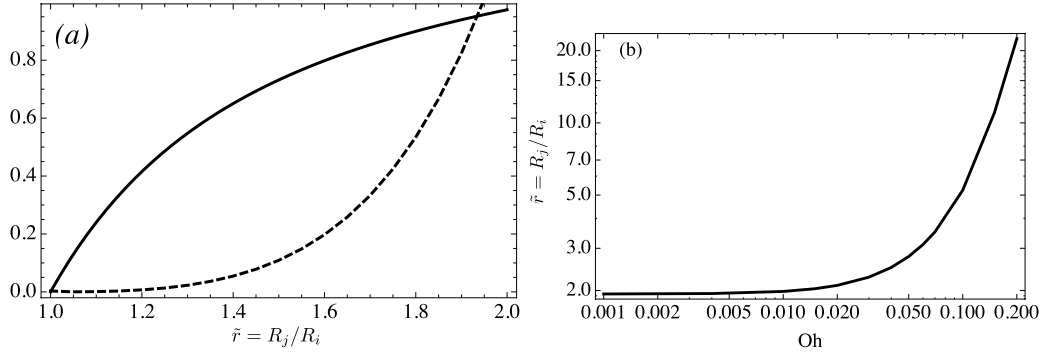


FIGURE 11. (a) Graphical determination of the selected ratio $\tilde{r} = R_j/R_i$ for $Oh = 10^{-3}$. The thick solid curve and the dashed curve are the l.h.s and r.h.s. functions of Eq. (4.4), respectively. (b) Selected ratio \tilde{r} as a function of the Ohnesorge number Oh .

5. Conclusion

In this article, we have reported a new kind of hydraulic jump mediated by capillary forces, instead of gravity. We have proposed a simple model for describing this hydraulic jump propagating along a Plateau border. The physics at play is controlled through the Weber and the Reynolds numbers. The analogy with hydraulics jump is evidenced by the existence condition $We > 1/2$. The propagation velocity and the profile are predicted through an equation describing the dynamics of a damped nonlinear oscillator. A simple and original experimental design has been proposed and implemented, which made the observation of these capillary jumps possible. All the measurements agree with the predictions of the theoretical approach, and confirm its validity, although we have never observed the solitary wave predicted by the model for $We < 1/2$, probably due to a too high viscosity of the liquid solutions.

Appendix A

In this appendix, we compute the averaged mean curvature (i.e. the mean curvature averaged over the azimuthal coordinate for a given cross-section) of the Plateau border. In Fig. 12.a, we show the cross section of the channel. The top interface is parameterized as an arc of a circle of radius $R(z)$:

$$x = R(z) \cos \phi \quad (\text{A } 1)$$

$$y = R(z) (\nu - \sin \phi), \quad (\text{A } 2)$$

where $\phi \in [\frac{\pi}{3}, \frac{2\pi}{3}]$, and $\nu = \frac{2}{\sqrt{3}}$. The diagonalization of the Hessian matrix on this surface yields the mean curvature :

$$H_g = -\frac{R(z)(1 - \nu \sin \phi)R''(z) - (-2\nu \sin \phi + \nu^2 + 1)R'(z)^2 - 1}{R(z)((\nu \sin \phi - 1)^2 R'(z)^2 + 1)^{3/2}} \quad (\text{A } 3)$$

Clearly, the variation of $R(z)$ induces a dependence of the curvature on the angular variable, as evidenced in Fig. 12b. This expression simplifies into

$$H_g = \frac{1}{R(z)} + \frac{1}{3} \left((3 + 2\sqrt{3}) \sin \phi - 3 \right) R''(z) \quad (\text{A } 4)$$

$$+ \frac{(-3(7 + 4\sqrt{3}) \sin^2 \phi + (6 + 4\sqrt{3}) \sin \phi + 8\sqrt{3} + 11) R'(z)^2}{6R(z)} + h.o.t., \quad (\text{A } 5)$$

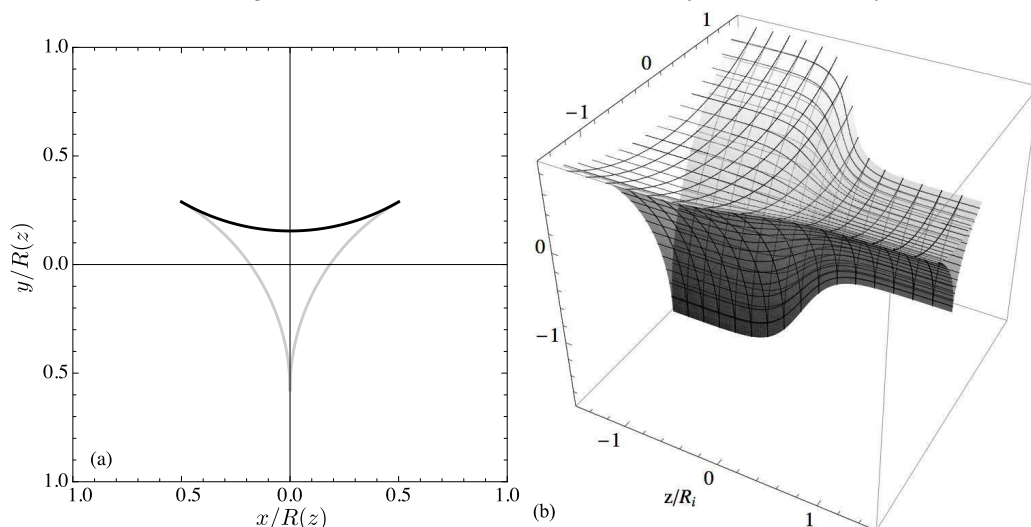


FIGURE 12. (a) Schematics of the cross section of the Plateau border. The thick curves represent the liquid-air interfaces. The thick black arc is the parameterized interface defined by the Eqs.(A 1),(A 2). (b) 3D sketch of the Plateau border defined with a hyperbolic tangent function for $R(z)$.

in the small slope limit. Since the model assumes no angular dependence, we average this relation between $\phi = \pi/3$ and $\phi = 2\pi/3$ and we finally get the averaged mean curvature within the mild slope approximation:

$$\kappa = \frac{1}{R(z)} + \beta_1 R''(z) + \beta_2 \frac{R'(z)^2}{R(z)} \quad (\text{A } 6)$$

where $\beta_1 = \frac{2\sqrt{3}-\pi}{\pi} \sim 0.103$ and $\beta_2 = \frac{3\sqrt{3}-\pi}{6\pi} \sim 0.109$

REFERENCES

- BÉLANGER, J. B. 1841 Notes sur l'hydraulique. *Ecole Royale des Ponts et Chaussées, Paris, France* **session 1842**, 223.
- BIDONE, G. 1819 Le remou et sur la propagation des ondes. *Report to the Royal Science Academy of Turin* **12**, 21–112.
- BOGY, D. B. 1979 Drop formation in a circular liquid jet. *Annual Review of Fluid Mechanics* **11**, 207–228.
- BOHR, T., PUTKARADZE, V. & WATANABE, S. 1993 Shallow-water approach to the circular hydraulic jump. *J. Fluid Mech.* **254**, 635–648.
- BOHR, T., PUTKARADZE, V. & WATANABE, S. 1997 Averaging theory for the structure of hydraulic jumps and separation in laminar free-surface flow. *Phys. Rev. Lett.* **79**, 1038–1041.
- BONN, D., ANDERSEN, A. & BOHR, T. 2008 Hydraulic jumps in a channel. *J. Fluid Mech.* **618**, 71.
- BOWLES, R. I. & SMITH, F. T. 1992 The standing hydraulic jump: theory, computations and comparisons with experiments. *J. Fluid Mech.* **242**, 145–168.
- BUSH, J. W. N. & ARISTOFF, J. M. 2003 The influence of surface tension on the circular hydraulic jump. *J. Fluid Mech.* **489**, 229–238.
- BUZZA, D. M. A., LU, C. Y. D. & CATES, M. E. 1995 Drop formation in a circular liquid jet. *J. Phys. II France* **5**, 37–52.
- CHANSON, H. 2011 *Tidal Bores, Aegir, Eagre, Mascaret, Pororoca. Theory and Observations*. World Scientific, Singapore.

- CHOW, V. T. 1959 *Open Channel Hydraulics*. McGraw–Hill.
- COHEN, A., FRAYSSE, N., RAJCHENBACH, J., ARGENTINA, M., BOURET, Y. & RAUFASTE, C. 2014 Inertial mass transport and capillary hydraulic jump in a liquid foam microchannel. *Phys. Rev. Lett.* **112**, 218303.
- CRAIK, A. D. D., LATHAM, R. C., FAWKES, M. J. & GRIBBON, P. W. F. 1981 The circular hydraulic jump. *J. Fluid Mech.* **112**, 347–362.
- DUCHESNE, A., LEBON, L. & LIMAT, L. 2014 Universal froude number in a circular hydraulic jump and its implication on the jump radius selection. *Phys. Rev. Lett.* .
- GÉMINARD, J.-C., ZYWOCINSKI, A., CAILLIER, F. & OSWALD, P. 2004 Observation of negative line tensions from plateau border regions in dry foam films. *Phil. Mag. Lett.* **84**, 199–204.
- HANSEN, F.K. & RØDSRUD, G. 1991 Surface tension by pendant drop: I. a fast standard instrument using computer image analysis. *J. Coll. Int. Sci.* **141**, 1–9.
- HIGUERA, F. J. 1994 The hydraulic jump in a viscous laminar flow. *J. Fluid Mech.* **274**, 69–92.
- JANNES, G., PIQUET, R., MAISSA, P., MATHIS, C. & ROUSSEAU, G. 2011 Experimental demonstration of the supersonic-subsonic bifurcation in the circular jump: A hydrodynamic white hole. *Phys. Rev. E* **83**, 056312.
- KAPITZA, P. L. 1948 Wave flow of thin viscous fluid layers. (english transl. in *Collected Works of P. L. Kapitza* (ed. d. ter haar) oxford: Pergamon (1965)). *Zh. Éksp. Teor. Fiz.* **18**, 3–28.
- KOEHLER, S. A., HILGENFELDT, S. & STONE, H. 1999 Liquid flow through aqueous foams: the node-dominated foam drainage equation. *Phys. Rev. Lett.* **82**, 4232–4235.
- KURIHARA, M. 1946 Laminar flow in a horizontal liquid layer. *Rep. of the Res. Inst. for Fluid Engng Kyusyu Imp. Univ.* **3-1946**, 11.
- LANDAU, L. D. & LIFSHITZ, E. M. 1987 *Fluid Mechanics*. Pergamon Press.
- LIGHTHILL, J. 1978 *Waves In Fluids*. Cambridge University Press.
- PASSANDIDEH-FARD, M., TEYMOURTASH, A. R. & KHAVARI, M. 2011 Numerical study of circular hydraulic jump using volume-of-fluid method. *J. Fluids Eng.* **133**, 011401.
- PITOIS, O., FRITZ, C. & VIGNES-ADLER, M. 2005 Hydrodynamic resistance of a single foam channel. *Colloids and Surfaces A; Physicochem. Eng. Aspects* **261**, 109–114.
- PRESS, W. H., TEUKOLSKY, S. A., VETTERLING, W. T. & FLANNERY, B. P. 2007 *Numerical Recipes 3rd Edition: The Art of Scientific Computing*, 3rd edn. New York, NY, USA: Cambridge University Press.
- RAUFASTE, C., FOULON, A. & DOLLET, B. 2009 Dissipation in quasi-two-dimensional flowing foams. *Phys. Fluids* **21** (5), 053102.
- RAYLEIGH, L. 1914 On the theory of long waves and bores. *Proc. R. Soc. Lond. A* **5**, 324–328.
- ROJAS, N., ARGENTINA, M., CERDA, E. & TIRAPEGUI, E. 2010 Inertial lubrication theory. *Phys. Rev. Lett.* **104**, 18780.
- ROJAS, N., ARGENTINA, M. & TIRAPEGUI, E. 2013 A progressive correction to the circular hydraulic jump scaling. *Phys. Fluids* **25**, 042105.
- SAVART, F. 1833 Mémoire sur le choc d’une veine liquide lancée contre un plan circulaire. *Ann. chim* **54**, 56–87.
- SIMPSON, J. E. 1997 *Gravity Currents: In the Environment and the Laboratory*, 2nd Edn. Cambridge University Press.
- TANI, I. 1949 Water jump in the boundary layer. *J. Phys. Soc. Japan* **4**, 212–215.
- WATSON, E. J. 1964 The radial spread of a liquid jet over a horizontal plane. *J. Fluid Mech.* **20**, 481–499.
- WEAIRE, D., PITTET, N., HUTZLER, S. & PARDAL, D. 1993 Steady-state drainage of an aqueous foam. *Phys. Rev. Lett.* **71**, 2670–2673.
- YOKOI, K. & XIAO, F. 2002 Mechanism of structure formation in circular hydraulic jumps: numerical studies of strongly deformed free-surface shallow flows. *Physica D* **161**, 202–219.